ISIJ International, Vol. 49 (2009), No. 10, pp. 1624–1629

Subsurface Fatigue Crack Generation and Strain Incompatibility Near Grain Boundaries for a Nitrogen-strengthened Austenitic Steel at Cryogenic Temperatures

Osamu UMEZAWA

Department of Materials Science and Engineering, Faculty of Engineering, Yokohama National University, 79-5 Tokiwadai, Hodogaya, Yokohama 240-8501 Japan.

(*Received on March 3, 2009; accepted on June 12, 2009*)

Fatigue damage in nitrogen-strengthened austenitic steel that showed subsurface crack generation and intergranular cracking at cryogenic temperatures has been characterized using electron backscatter diffraction (EBSD) analysis. Strain gradients near grain boundaries and localized stress concentrations in grains were clearly detected. The strain gradient in the vicinity of a grain boundary accompanied a misorientation of a few degrees, and may result from co-planar dislocation arrays at the grain boundary. To reduce localized strain incompatibility at grain boundaries, fine-grained duplex microstructure was obtained through partial recrystallization. The treated material showed considerably improved high-cycle fatigue strength and more homogenous plastic deformation.

KEY WORDS: high-cycle fatigue; subsurface crack initiation; co-planar arrays; austenitic steel; electron backscatter diffraction.

1. Introduction

Subsurface fatigue crack initiation occurs without any defects in titanium alloys[1–3] and austenitic steels[4] at cryogenic temperatures. It was dominant in the long-life range at lower temperatures,[5] while surface cracks are initiated in high peak stress and low cycle fatigue tests. Thus, the initiation site shifts from the surface to the interior at the low stresses where it is well below the macro-yield range. The subsurface crack initiation sites in each alloy are highly crystallographic as transgranular[1–3] or intergranular cracking.[4] It has been pointed out that the localized deformation and/or stress concentration in the vicinity of grain boundaries due to dislocation arrays is not only potential sources of microcracking, but also that a specific region (weakest-link) with microstructural heterogeneity provides a potential site against strain incompatibility and microcrack generation.[1–6] Freudenthal[7] defined that high strength materials showing the deformation manners such as co-planar arrays were pseudo-elastic materials. In contrast, plastic materials such as copper were defined as those in which the micro-slip was extensive and diffuse and where surface distortions produced by the reversed slip were the primary nuclei for macro-crack generation. Extrusion–intrusion (persistent slip bands) models represent fairly well for the plastic materials, but not for the *pseudo*-elastic materials in the high-cycle regime. Heterogeneous microplasticity occurring planar slip and restricted slip systems in a specific region is considered to play an important role in the subsurface crack generation. Elastic anisotropy, crystal orientation, heterogeneity of a slip system and elastic binding between the neighboring grains produce elastic incompatibility between grains.[3]

In the previous study,[4] the dislocation structure and subsurface crack initiation sites of nitrogen-strengthened austenitic steels were evaluated. The subsurface crack initiation sites were formed intergranularly. The main deformation mode was $\{111\}$–$\langle 110\rangle$ sliding, and piled-up dislocation arrays were observed on the identical slip plane. In the vicinity of grain boundary, a secondary slip system was also activated, and stress concentration was detected. It is considered to be geometrically necessary (GN) dislocation[8] in the many transpositions that has formed and observed in the local strain gradient. Thus, localized deformation due to dislocation arrays must promote intergranular cracking owing to the incompatibility at grain boundaries. Transmission electron microscopy (TEM) characterization of fatigue damage, however, is performed with high magnification; it is difficult to understand the outline of the polycrystalline grains due to the constraints imposed by the diffraction conditions.

In this study, electron backscatter diffraction (EBSD) in scanning electron microscopy (SEM) was then used to analyze the grain-boundary characteristic distribution of the relative strain, and crystal orientation in the polycrystalline grains after fatigue deformation for solution-treated 24Cr–15Ni–4Mn–0.3N austenitic steel. Furthermore, a novel treatment that consisted of cold grooved-rolling and partial recrystallization (PR) was introduced to modify the microstructure of the steel.[9] Both the refinement of the grain

structure and the introduction of mobile dislocations on various slip systems may be effective to decrease the incompatibility at grain boundaries, thus resulting in high fatigue resistance against subsurface crack generation.[10)]

2. Experimental Procedure

2.1. Fatigue Test Conditions and Samples

The test material was nitrogen-strengthened austenitic steel under solution-treated (ST) conditions. The major chemical constituents of the steel were 0.022 mass% of C, 0.97 mass% of Si, 4.14 mass% of Mn, 14.74 mass% of Ni, 24.43 mass% of Cr, 0.33 mass% of N, and Fe (remaining amount). The tensile properties were summarized in the reference.[4)] The longitudinal direction of the hourglass-type specimens was perpendicular to the hot-rolling direction. Load-control fatigue tests were carried out at 4 K and 77 K. The loading was uniaxial with a minimum-to-maximum stress ratio of $R=0.01$.

Figure 1 shows the S–N data.[4)] The analyzed samples were fatigue-fractured specimens that exhibited subsurface crack generation. The fatigue-fractured specimens were cut off along the longitudinal section. Its section line was almost parallel to the initial-crack propagation direction and to the principal stress axis. The analysis area was beneath the fracture surface in the Stage II region. The section was mechanically polished and was prepared by a conventional electrical jet-polishing technique in a stirred solution of 10% perchloric acid and 90% acetic acid at approximately 290 K.

2.2. Electron Backscatter Diffraction Analysis

Orientation imaging microscopy, which was based on EBSD in SEM, was performed to determine the misorientation and strain distribution in the microstructure. The microscope used was JEOL JSM-6400 equipped with a LaB_6-type gun. A data set of point analyses with every 0.2–1.0 μm beam scanning in hexagonal grids (pixels) for both X and Y (parallel to the principal stress axis) directions yielded maps of the parameters such as the image quality (IQ), inverse pole figure (IPF) and confidence index (CI). The IQ represents diffraction-pattern intensity and reflects the strain field.[11)] A CI ranging from 1 (perfect) to 0 statically indicates the reliability of the orientation determined for each point.

2.3. Partial Recrystallization

The rectangular bar with 30-mm-square, which was obtained by cutting the test material in the transverse direction, was formed into rods with a diameter of 14 mm by multi-steps grooved-rolling and swaging. The true strain in total reduction was approximately 1.8. A cold-worked material was heat treated at 1 073 K for 3.6 ks and this was followed by water quenching to obtain a partially recrystallized (PR) structure.[9)]

3. Results

3.1. Microstructure

The grain boundary (misorientation) image by EBSD for the ST material was obtained with sharp line as shown in

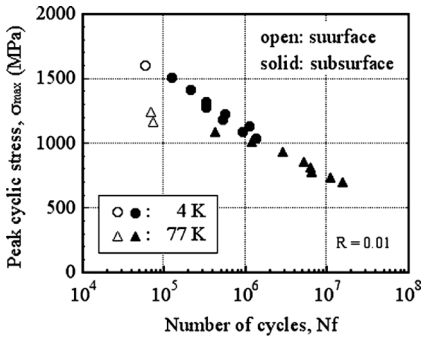

Fig. 1. S–N data of the test material at cryogenic temperatures.

Fig. 2(a). A small-angle (SA, which is blue in color; less than 15°) boundary, a large-angle (LA, which is black in color) boundary without $\Sigma 3$ (greater than 15°), and a $\Sigma 3$ coincidence-site lattice (CSL, which is red in color) boundary are clearly recognized. Among LA boundary at the area of 1×1 mm, the ratio of $\Sigma 3$ annealing twin boundary was approximately 38%, and other CSL boundaries could hardly be detected. The minimum misorientation of the SA boundary is defined as 1° (a) and 0.5° (b) in Fig. 2. These images show that the resolution of misorientation is less than 1°.

3.2. Orientation Imaging Analyses for Fatigued Samples

Figure 3 shows an orientation map indexed by IPF for CI>0.1 (a) and a misorientation map (b) for a sample fractured at high stress level at 4 K. Low CI values (CI<0.1, black points) are mostly distributed beneath the fractured surface (up to a depth of approximately 100 μm) and grain boundaries. The occurrence of plastic deformation is severe in the grains just beneath the fractured surface, even when the stress level is higher than 0.2% proof stress. Misorientations between pixels with a few degrees (blue color) and more (red color) in some grains were detected as shown in (b). Such area also involved low CI values as shown in (a). These misorientations and low CI values must be correlated with a localized plastic deformation.

Figure 4 shows an IQ map (a) and an IPF map (b) for a sample fractured at a low stress level at 4 K (0.2% proof stress: $\sigma_{0.2}=1\,308$ MPa). Two types of boundaries are shown in the IQ map: one is a sharp line, and the other is a broad one. The broad-line image is considered to represent the strain gradient near its grain boundary, since IQ indicates the strain field in the crystal. A poor IQ regime in a grain (marked area shown in Fig. 6(d)) was also observed at a neighboring grain boundary junction. A shear strain gradient should be followed by lattice rotation, and some regions are analyzed in detail in the following discussion. In the orientation map (b), data points with a value of CI less than CI=0.2 were cut off. The black-colored points were mainly detected at the LA boundary. The region with a low CI at $\Sigma 3$ boundary was limited and the CI value was less than that at the LA boundary.

Figure 5 shows the IPF map and misorientation map of a fractured sample at the lowest stress level ($\sigma_{0.2}=973$ MPa, 77 K). Around the grain boundary junction, a fold in a grain was clearly detected as indicated by an arrow in Fig. 5(a).

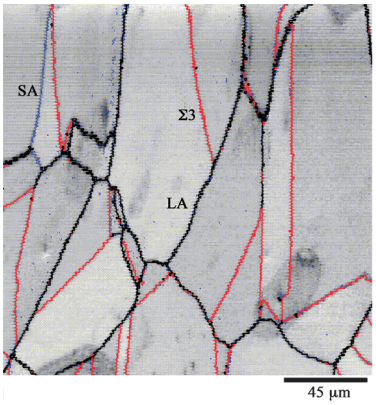

(a)

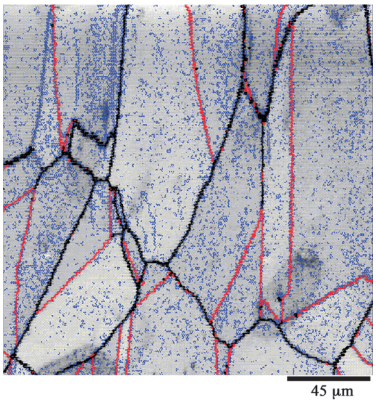

(b)

Fig. 2. Image quality map of solution treated material with misorientation: blue color for small angle boundary (SA, less than 15°), black color for large angle boundary (LA, more than 15°) and red color for Σ3 CSL boundary (Σ3). Minimum misorientation of SA is defined as 1° (a) and 0.5° (b).

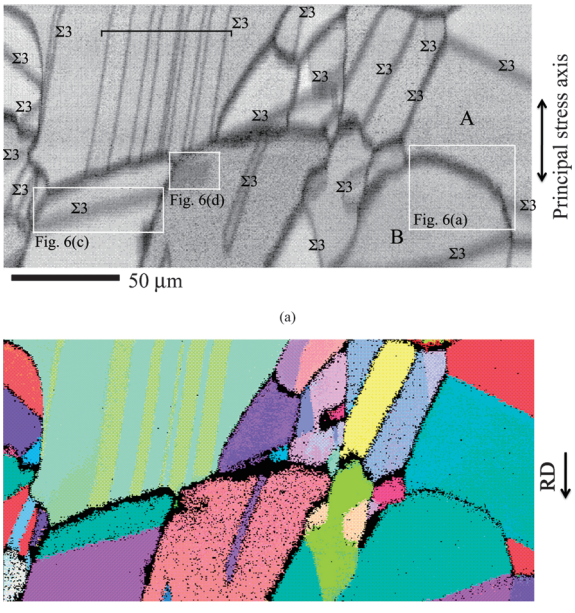

(a)

(b)

Fig. 4. IQ map (a) and IPF map cut off points less than CI=0.2 normal to RD direction (b) in the transverse section of a fatigued sample at 4 K (σ_{max}=1 084 MPa, Nf=939 610 cycles).

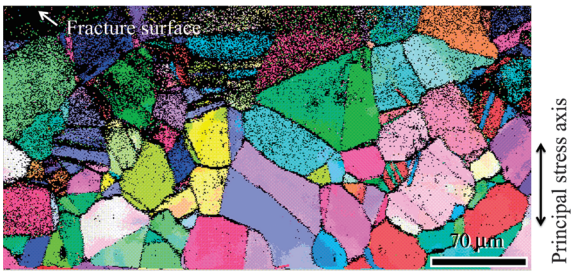

(a)

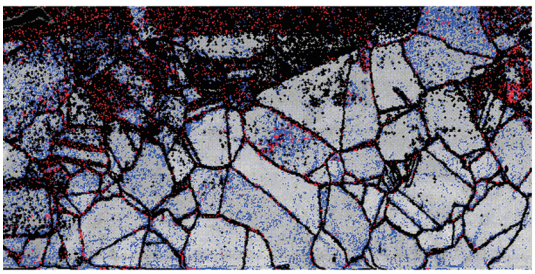

(b)

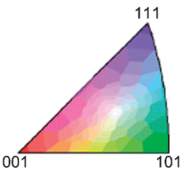

(c)

Fig. 3. IPF map cut off points less than CI=0.1 (a) and misorientation map (b) of beneath the fractured surface in the transverse section (4 K, σ_{max}=1 508 MPa, Nf=127 360 cycles). Boundary levels in (b) are defined as 1°–2° with blue, 2°–15° with red and more than 15° with black. Color index of IPF is defined as (c).

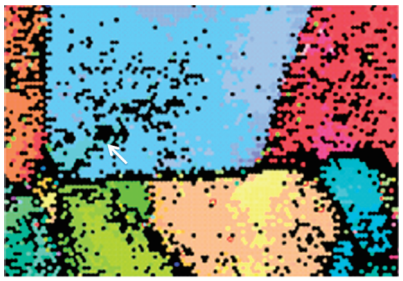

(a)

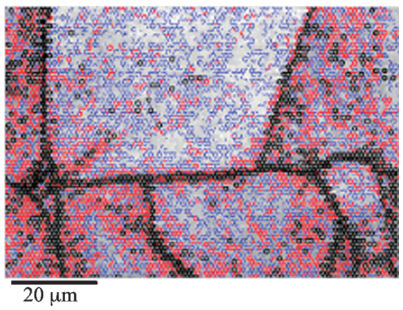

(b)

Fig. 5. IPF map cut off points less than CI=0.1 (a) and misorientation map (b) in the transverse section of a fatigued sample at 77 K (σ_{max}=691 MPa, Nf=16 240 650 cycles). An arrow in (a) indicates the fold. Boundary levels in (b) are defined as 0.5°–1° with blue, 1°–15° with red and more than 15° with black.

The strain-gradient near the grain boundary junction and localized stress concentration in a grain were observed even at low stress levels.

4. Discussion

4.1. Strain-gradient Near Grain Boundaries

TEM studies have confirmed that the glide process is extremely planar.[4] The dislocation movements on their slip planes were restricted, and the cross-slip of the dislocations was strongly suppressed. The dislocation arrangement was mainly developed due to pile-ups or co-planar arrays, which were blocked at the grain boundary at low stress levels. Although the slip bands were not well formed, the micro-slip bands were widely spaced. Even at the low stress levels, dislocations were generated in a grain with more than one slip system; however, their densities were rather low.

The poor IQ region along a grain boundary shown in **Fig. 6**(a) shows a strain gradient near the grain boundary, with misorientations of a few degrees for each pixel as red color lines shown in Fig. 6(b). The misorientations between pixels were also distributed in grain A rather than in grain B. The poor IQ region along the grain boundary was mostly located in grain B. The grain boundary between grains A and B was an LA boundary and their rotational axes were almost parallel to the stress axis (RD), as shown in Fig. 4(b). It is deduced that coplanar dislocation arrays developed in grain A were blocked at the grain boundary and this led to a strain incompatibility at the boundary. Consequently, an elastic strain was introduced in grain B along the boundary, since the deformation between grains should be continuous without slip transfer. Therefore, low CI values were limited to the boundary, and the low IQ region resulted from elastic bending.

In some $\Sigma 3$ boundaries, no poor IQ region was observed, as shown in Fig. 4(a); this was probably because direct slip transfer was available under an orientation condition between the coplanar slips and the boundary. In other $\Sigma 3$ boundaries, a poor IQ region extended on both sides of the grains, as shown in Fig. 6(c). However, misorientations (lattice rotations) were hardly detected in the region. This was probably because of the interaction between $\Sigma 3$ boundary and impinging slip to emit grain boundary dislocations and slip in the neighboring grain.

At neighboring boundary junctions with LA, poor IQ region was detected at not only along LA but also into a gain as shown in Fig. 6(d). The region was corresponded to low CI one. The reason why larger misorientations between pixels were detected in the region may result from poor quality EBSD pattern due to stress concentration. The boundaries junction gives a potential site to induce localized stress concentration as well as the fold shown in Fig. 5.

4.2. Strain Incompatibility Due to Heterogeneous Slip

Cyclic strain curves for a large group of metals are independent of the loading and heat treatment history. This is especially true for pure metals with a high stacking fault energy in which cross-slip occurs easily and which is characterized by a wavy slip. Increasing the number of mobile dislocations caused cyclic softening in the high cycle range at a stress well below the macro-yield range.[12] Feaugas and

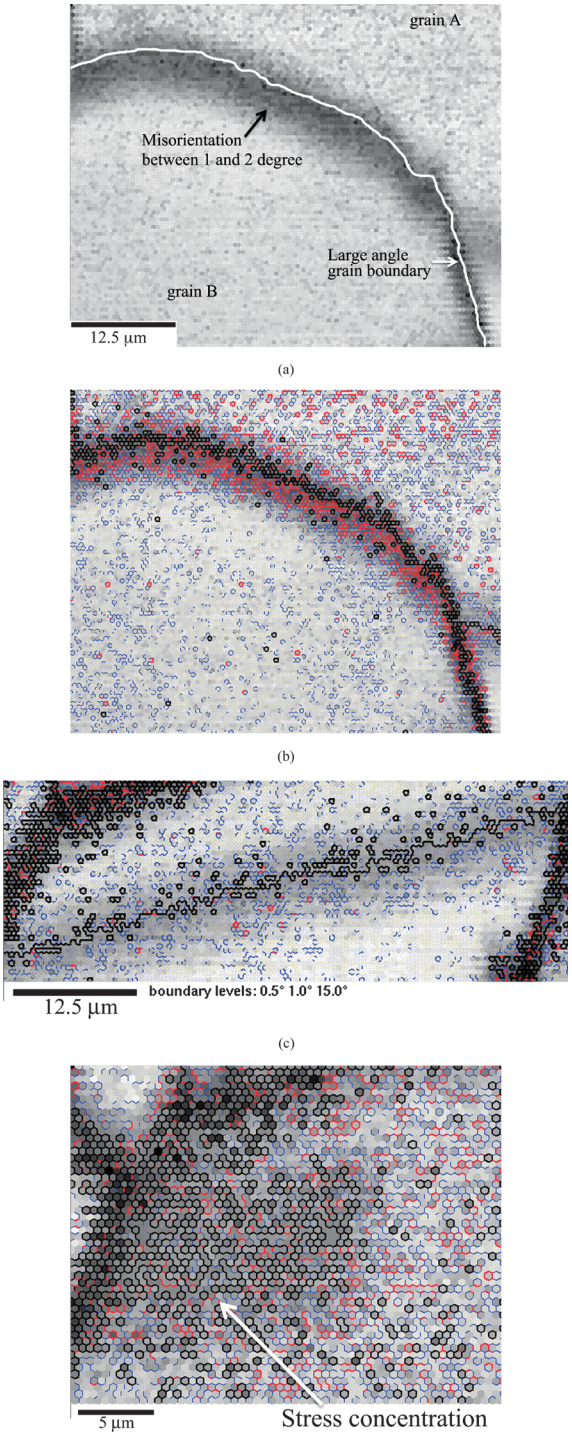

Fig. 6. Misorientation analyses for a large angle boundary (a, b), a $\Sigma 3$ boundary (c) and a stress concentrated region near boundary junction (d) in Fig. 4. Boundary levels are defined as 0.5°–1° with blue, 1°–15° with red and more than 15° with black.

Clavel[13] reported that cyclic softening resulted from a decrease in the back-stress component. The larger the cyclic strain amplitude that pseudoelastic materials can sustain before wide spread macroscopic yielding, the more severe the localized stresses will be around the strain incompatibilities.[7] Let us consider the reason for the occurrence of microcracking when cyclic softening is accompanied by coplanar dislocation pile-ups.

It has been suggested that facet formation requires a crit-

ical combination of shear stress and tensile stress in the cracked plane.[3] This idea is applicable to not only transgranular cracking but also intergranular one. Line traces that indicated the presence of slip systems were detected on only one side of the intergranular facet at a subsurface crack initiation site.[4] There were no traces on the other side. It was believed that strain incompatibility at the grain boundary, not the brittle cracking, caused intergranular fracture. When a slip is introduced in a grain, the slipped area becomes softer than non-slipped area because of an increase in mobile dislocations. Hence necessary slips may be localized near the first slip plane. This localized slip plane may be the softest because of its crystallographic orientation. The coplanar arrays developed in a grain under the cyclic softening impinge the grain boundary and produce steps and/or protrusions, which produces a strain-gradient in the neighboring grain as described in above. Thus the strain incompatibility containing shear strain field at the grain boundary is believed to be developed and to act shear stress and tensile stress to the grain boundary plane, since the grain boundary plane is inclined to the applied stress axis. In order to relax the strain incompatibility, therefore, a slip or microcracking must occur between the neighboring grains.

4.3. Microstructural Control to Decrease Strain Incompatibility at Grain Boundaries

The S–N curve of the ST material was classified into the two parts that were attributed to different mechanisms of fatigue crack generation.[5] A microstructural design to improve the high-cycle fatigue strength or fatigue limit was proposed in a previous study.[10] **Figure 7** shows an illustration of S–N curves obtained for the proposed design. Grain refinement and the remaining damage introduced by the cold-work step provided high tensile strength to the partially recrystallized (PR) material. However, the increase in the fatigue strength in the low-cycle regime was relatively low and not proportional to the increase in the tensile strength. The damage in the PR material may accelerate plastic-strain accumulation. On the contrary, the grain boundary embrittlement against strain incompatibility should be considered in the high-cycle regime, since the weakest link of grain boundaries is adopted for studying the subsurface fatigue crack generation. The grain refinement and pre-existing dislocations may assist rather homogeneous deformation and reduce the strain incompatibility at grain boundaries. Then, subsurface crack generation resulting from intergranular cracking disappears, and the fatigue strength in the high-cycle regime increases.

For the test alloy, the PR material was successful in decreasing the maximum size of the grain. **Figure 8** shows the microstructure of transverse and longitudinal sections. Regions A, B, and C represent recrystallized grains, microduplex grains, and deformed grains, respectively. The recrystallized grains were about 10 μm in size and particles with less than a few hundred nm in diameter were distributed in the grains. The microduplex structure was consisted of grains with a few μm in size and particles with several nm.[9] Those particles were estimated as σ-phase precipitates.[9] The PR showed a higher fatigue strength than the ST, especially in the high-cycle regime, as shown in **Fig. 9**. Dislocation structure developed in the fatigued PR samples showed multidirectional plastic deformation in the region A

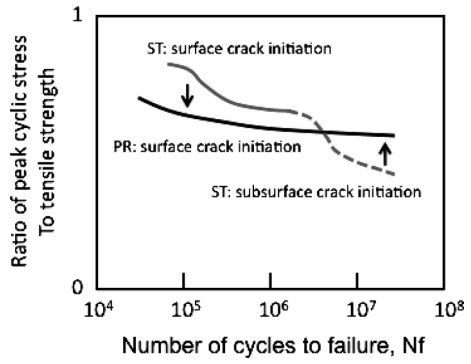

Fig. 7. Schematic S–N curves showing modification by partial recrystallization.

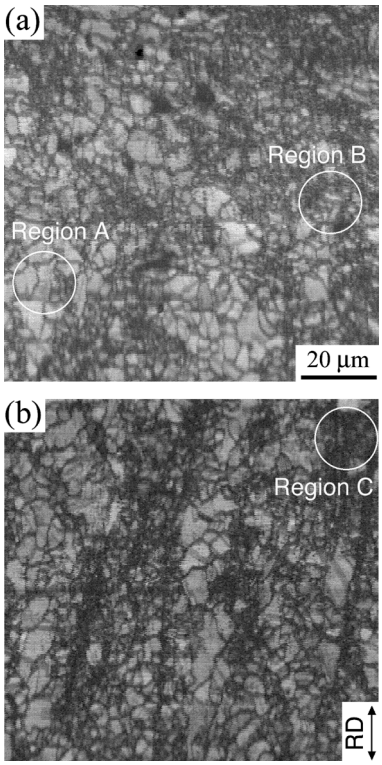

Fig. 8. Image quality maps of PR material showing three grain regions, A, B and C: (a) transverse section and (b) longitudinal one.

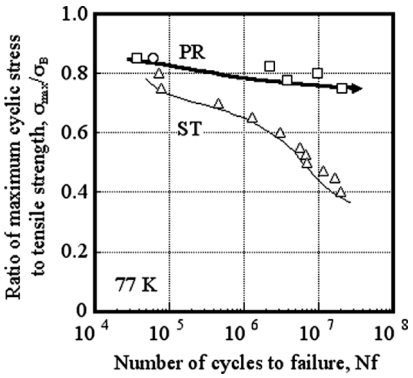

Fig. 9. S–N data normalized by tensile strength of the PR and ST materials at 77 K (ultimate tensile strength σ_B: 1 713 MPa in the PR and 1 535 MPa in the ST).

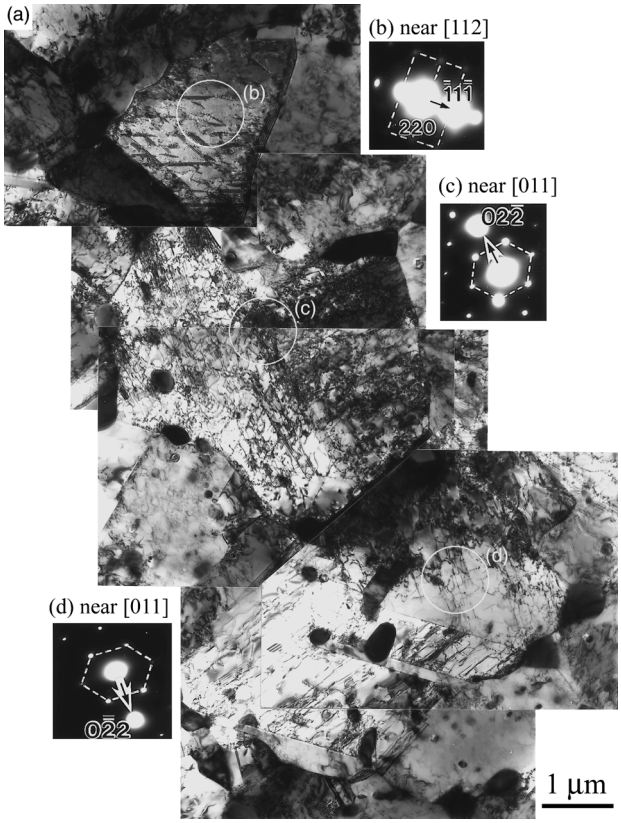

Fig. 10. Bright field image of the dislocation structure in the Region A for a fatigued PR material (stress amplitude: σ_a=661 MPa, Nf=9 401 610 cycles) (a), and selected area diffraction patterns (b)–(d). Each diffraction pattern is taken from white circle area shown in photograph (a). Photograph (a) is a combined image with three images under slightly different beam conditions of (b)–(d).

as shown in **Fig. 10**, although heterogeneous dislocation arrays were developed in the ST as described in the previous study.[4] It has been successfully demonstrated that multiple slips developed in considerable number of grains promote homogeneous and multi-directional plastic deformation so that the localized deformation and strain incompatibility at grain boundaries must be reduced.

5. Conclusions

Fatigue damage in nitrogen-strengthened austenitic steel, which showed subsurface crack generation of intergranular cracking at cryogenic temperatures has been characterized using SEM-EBSD analysis. The major results of this characterization are summarized below.

(1) Severe plastic deformation occurred in the grains just beneath the fractured surface even at the stress levels higher than 0.2% proof stress. Misorientations between pixels with a few degrees and more in some grains were detected in neighboring grains.

(2) The strain gradient near the grain boundary and the localized stress concentration in a grain were clearly detected, where the IQ and CI showed a low value. The strain gradient in the vicinity of a grain boundary accompanied a misorientation of approximately 1 degree for each pixel, and it may result from the stress concentration resulting from the presence of coplanar dislocation arrays in the neighboring grain.

(3) In order to reduce the localized strain incompatibility at grain boundaries, a fine-grained duplex microstructure was obtained through PR. The treated material showed considerably high fatigue strength, especially in the high-cycle regime and revealed a greater extent of homogenous plastic deformation. The multiple slips that developed in a considerable number of grains may promote homogeneous and multidirectional plastic deformation; further, the localized deformation and strain incompatibility at grain boundaries were believed to decrease as a result of the treatment.

REFERENCES

1) O. Umezawa, K. Nagai and K. Ishikawa: *Mater. Sci. Eng. A*, **A129** (1990), 217.
2) O. Umezawa, K. Nagai and K. Ishikawa: *Tetsu-to-Hagané*, **76** (1990), 924.
3) H. Yokoyama, O. Umezawa, K. Nagai, T. Suzuki and K. Kokubo: *Metall. Mater. Trans. A*, **31A** (2000), 2793.
4) O. Umezawa and K. Nagai: *Metall. Mater. Trans. A*, **29A** (1998), 809.
5) O. Umezawa and K. Nagai: *ISIJ Int.*, **37** (1997), 1170.
6) O. Umezawa, K. Nagai and K. Ishikawa: *Mater. Sci. Eng. A*, **A129** (1990), 223.
7) A. M. Freudenthal: *Eng. Fract. Mech.*, **6** (1974), 775.
8) M. F. Ashby: *Philos. Mag.*, **21** (1970), 399.
9) O. Umezawa: *CAMP-ISIJ*, **17** (2004), 1346.
10) O. Umezawa: *Metall. Mater. Trans. A*, **35A** (2004), 543.
11) O. Umezawa: *J. Jpn. Inst. Light Met.*, **50** (2000), 86.
12) R. K. Steele and A. J. McEvily: *Eng. Fract. Mech.*, **8** (1976), 31.
13) X. Feaugas and M. Clavel: *Acta Mater.*, **45** (1997), 2685.